

Electronic structure of B_2O_3 glass studied by one- and two-dimensional electron-spin-echo envelope modulation spectroscopy

Yiannis Deligiannakis, Loukas Astrakas, and George Kordas

Institute of Materials Science, National Center for Scientific Research Demokritos, 15310 Aghia Paraskevi Attikis, Greece

Robert A. Smith

US Borax Incorporated, 26877 Tourney Road, Valencia, California 91355-1847

(Received 3 February 1998)

B_2O_3 in glass and crystalline states have been subjected to γ irradiation at room temperature and subsequently studied by continuous-wave electron paramagnetic resonance and electron-spin-echo envelope modulation (ESEEM) spectroscopy at liquid-helium temperature. The ESEEM study of B_2O_3 revealed the existence of weak magnetic couplings between the irradiation-induced paramagnetic centers and nearby ^{10}B , ^{11}B nuclei. The assignment of the observed couplings was achieved by the use of the two-dimensional hyperfine sublevel correlation spectroscopy. A detailed theoretical analysis of the ESEEM spectra and a $S = \frac{1}{2}$, $I = \frac{3}{2}$ system in both time and frequency domain is also presented. Computer simulation of the spectra, Hartree-Fock self-consistent field, and modified neglect of differential overlap calculations revealed that the unpaired electron in the B_2O_3 glass is associated with a dangling bond of oxygen attached to a boron of a boroxol ring. The paramagnetic centers of the B_2O_3 crystal are associated with oxygen dangling bonds in boron trigonal units. Pertinent structural models for the glass B_2O_3 are examined at a microscopic level. [S0163-1829(98)01341-1]

INTRODUCTION

In B_2O_3 glass, boron and oxygen form a variety of structural units, depending upon the alkali metal concentration. Krogh-Moe¹ provided considerable evidence for the existence of various structural assemblages in borate glasses. The boroxol group is the characteristic structural unit of pure boron-oxide glass.¹ In the presence of alkali oxides other units can be formed such as pentaborate, triborate and diborate groups.¹ Nuclear magnetic resonance (NMR) data show that within the B_2O_3 glass the boron atoms can be either fourfold- and threefold-coordinated with bridging oxygens, or threefold coordinated with either one or two nonbridging oxygens.^{2,3} In $^{11,10}B$ -enriched^{2,4} and ^{17}O -enriched⁴ B_2O_3 glasses, NMR data show the existence of ring and nonring sites. Neutron-scattering data in vitreous B_2O_3 indicated the existence of boroxol rings⁵ and that 60% of the boron atoms are included in boroxol rings.⁶ The existence of planar boroxol rings in B_2O_3 glass was also evidenced by Raman spectroscopy in borate glasses.⁷⁻⁹ Thus it seems that there is ample evidence that in B_2O_3 glass the boron atoms are in trigonal sites most of them (60%) belonging to boroxol groups and the rest to connecting B_2O_3 units. In contrast to the glass B_2O_3 , in crystalline B_2O_3 no boroxol rings are present. NMR (Ref. 10) and x-ray¹¹ data show that in the crystalline state the boron atoms have planar trigonal coordination.

Irradiation-induced paramagnetic centers in glass can be studied by EPR and thus serve as sensitive probes of the local structure.¹² So far, the main body of data in irradiated borate glasses comes exclusively from continuous-wave EPR studies, reviewed in Ref. 12. The continuous-wave EPR spectrum of γ -irradiated B_2O_3 glass is inhomogeneously broadened mainly by distribution of the g values and the

anisotropic hyperfine coupling. The main features of the c.w. EPR spectrum consisting of "five lines plus shoulder" has been assigned to the hyperfine coupling (~ 35 MHz) between the electron spin and a single $^{11}B(I = 3/2)$ nucleus.¹³⁻¹⁵ This boron hyperfine coupling is considered to originate from a spin-polarization mechanism.¹³⁻¹⁵ However a quantitative analysis of this phenomenon is still lacking. In crystalline B_2O_3 the observed EPR spectrum has the same basic features as in glass¹⁵ including the low-field shoulder. In the glass, the observed low-field broad shoulder in the EPR spectrum had been attributed to a distribution of the corresponding g values most likely due to local disorder effects.¹³ Such an explanation is not adequate for the crystalline material since in this material there is no disorder.

In summarizing, the c.w. EPR data allow the resolution of a single, strongly coupled boron nucleus. Weaker hyperfine couplings and/or possible quadrupole couplings cannot be resolved since their effects are hidden underneath the inhomogeneous broadening. In B_2O_3 weak hyperfine couplings are expected for distal boron nuclei, i.e., those located at three or more bonds away from the paramagnetic oxygen. The couplings for these nuclei are expected to be sensitive to the structural details and this renders them sensitive probes of the structural and electronic properties of B_2O_3 glass. The electron-spin-echo envelope modulation (ESEEM) spectroscopy,^{16,17} which is a pulsed EPR technique, is eminently suited for measuring low-nuclear spin-resonance frequencies¹⁶⁻¹⁸ offering a powerful tool for the detailed study of the microenvironment of the paramagnetic centers in solids. If a nuclear spin is coupled via hyperfine interaction with the electron spin then, a formally forbidden nuclear-spin-flip transition ($\Delta M_S = \pm 1$, $\Delta m_I \neq 0$) is partially allowed due to state mixing.¹⁶ In general, this state mixing is strongly angular dependent. ESEEM arises from interference

effects between allowed and forbidden transitions, both of which are excited by intense microwave pulses and it is observed as a periodic variation of the echo intensity. In single-crystal samples the modulation contains the nuclear-transition energies. In randomly oriented samples, the ESEEM spectrum is a superposition of spectra from many different orientations each with different nuclear frequency and different modulation depth. In general, due to the strong angular dependence of the state mixing, and thus the modulation depth, a spectrum from which the principal values of the hyperfine coupling tensor(s) can be easily assigned, is not obtained. Computer simulations are required for the proper analysis of the spectra. Nevertheless, it is well documented that for nuclei with $I=1/2$ or $I=1$ an isotropic hyperfine coupling A_{iso} which “matches” the nuclear Larmor frequency ν_I , i.e., when $A_{\text{iso}}=2\nu_I$, leads to well-resolved ESEEM spectra from which the hyperfine and the quadrupole coupling tensors can be evaluated in a straight manner.¹⁷ In cases of complex overlapping ESEEM spectra the four-pulse two-dimensional hyperfine sublevel correlation spectroscopy¹⁹ (2D-HYSCORE) has been shown to be a promising method for elucidating the hyperfine couplings.^{20–23}

In the case of an electron spin interacting with a nuclear spin $I=3/2$, the ESEEM spectra are complicated.²⁴ The existing experimental ESEEM work for $I=3/2$ is rather scarce and refers to nuclei with either very weak (⁷Li nuclei),^{25,26} or very strong quadrupole coupling (^{37,35}Cl nuclei).²⁷ Up to now, the application of the ESEEM technique to the study of paramagnetic centers in glasses is fairly limited.^{28,29,25,30,31} Recently, Kordas²⁸ introduced the pulsed-EPR spectroscopy in the $(100-x)\text{B}_2\text{O}_3x\text{Li}_2\text{O}$ (x =mole percentage) system with $x=0-50$, in a preliminary fashion.

In the present work we report an ESEEM study of γ -irradiated B₂O₃ glass. Our motivation was primarily to get a detailed understanding of the environment of the irradiation-induced paramagnetic centers. In contrast to the continuous-wave EPR spectroscopy, the present ESEEM measurements can resolve the magnetic coupling between the electron spin and ¹⁰B, ¹¹B nuclei located more than two bonds away from the paramagnetic oxygen. The application of the 2D-HYSCORE technique for B₂O₃ allowed the resolution and assignments of these weak boron hyperfine couplings. The ESEEM data for B₂O₃ are discussed in terms of possible structural units in the borate glass. The assignments were supported by molecular orbital (MO) calculations using the modified neglect of diatomic overlap (MNDO) VAMP 4.4 Erlangen convex computer version, AMPAC SEMICHEM PC-version and Hartree-Fock self-consistent field (HF-SCF) GAUSSIAN 94 programs. These programs were used to calculate the spin densities and equilibrium structures of the boron-oxygen related units. The two programs are explained in other papers.³²

EXPERIMENT

Sample preparation: B₂O₃ glasses (more than ten melts) have been prepared by the melting technique in a platinum crucible. B₂O₃ crystal was prepared by the method of Kline *et al.*¹⁰ using boron phosphate as a seed. The final batch of crystals contained 44 ppm phosphorous as analyzed by ICP

and the x-ray powder pattern, characterized with a Philips X’Pert MRD, was identical with JCPDS 44-1085.

Molecular orbital calculations: At first, a MNDO PC-version of AMPAC was used to obtain an optimized structure of boroxol rings. Second, the VAMP4.4 program was used to reproduce the AMPAC calculation using a CONVEX super-computer. The optimization of the structure was repeated using the GAUSSIAN 94 program. The calculations were done using 6–311 G basis set at B3LYP levels of theory to allow the determination of spin-polarization contributions.³³ The GAUSSIAN 94 computes hyperfine splitting constants as a part of the population analysis expressed in atomic units given in the section “Fermi contact analysis.” The conversion from a.u. to MHz occurs using the expression $b_F=8/3g_e g_I K B_F$ where g_e is the free-electron factor equal to 2.0023, K is a conversion factor equal to 47.705336 MHz, B_F is the computed hfs parameter in a.u. from the Gaussian 94 analysis, and g_I is the nuclear gyromagnetic ratio for the atom type in question. The g_I values used for H^1 and B^{11} are 5.585 691 2 and 1.792 424, respectively.

Spectroscopic measurements: Continuous-wave (c.w.) EPR spectra were recorded at liquid-helium temperatures with a Bruker ESP 380 X-band spectrometer operating in the c.w. mode, equipped with an Oxford Instruments cryostat. The microwave frequency was measured with a microwave frequency-counter HP 5350B.

Pulsed EPR was performed with the Bruker ESP 380 spectrometer equipped with a dielectric resonator and a BRUKER ESP380-1078 IN echo integrator. The instrument dead time was about 100 ns. For the field-swept spectra the echo integral was recorded as a function of the magnetic field after a two-pulse sequence ($\pi/2$ -144 ns- π). The duration of the $\pi/2$ and π pulse was 64 and 128 ns, respectively. In the three-pulse ($\pi/2$ - τ - $\pi/2$ - T - $\pi/2$) ESEEM data the amplitude of the stimulated echo as a function of $\tau+T$ was measured at a frequency of 9.71 GHz at a magnetic field corresponding to the maximum intensity of the field-swept spectrum. The minimum interpulse T was 40 ns and was incremented in steps of 8 ns. The duration of the $\pi/2$ pulse was 16 ns. Measurements were carried out at 25 K with a repetition rate of 5 Hz and τ values from 120 to 600 ns. 2D-HYSCORE spectra were recorded using the sequence ($\pi/2$ - τ - $\pi/2$ - t_1 - π - t_2 - $\pi/2$ -echo), where the echo is measured as a function of t_1 and t_2 .¹⁹ The duration of the $\pi/2$ and π pulse was 16 and 32 ns, respectively, with equal amplitudes. 128–150 points were recorded in each dimension for a series of τ values from 104 to 368 ns, while the t_1 and t_2 were incremented in steps of 16 ns from their initial value. To remove the unwanted echoes, the appropriate phase-cycling procedures in the stimulated-echo³⁴ and HYSCORE (Ref. 35) experiments were applied.

Data manipulation: (i) *1D-stimulated echo ESEEM:* The experimental spectrum was normalized to the time-zero echo intensity which was estimated by dead-time reconstruction by the linear prediction singular value decomposition method.²⁹ Prior to Fourier transform the time-domain echo decay was factored out by subtraction of a linear function and zero filling to 512 points was performed followed by a tapering with a Hamming window. (ii) *2D-HYSCORE ESEEM:* The background decay in both t_1 and t_2 dimensions was subtracted using a linear function followed by zero

filling to 512 points in two dimensions and tapering with a Hamming window; then Fourier transform was carried out in both dimensions.

Simulation of ESEEM spectra: The spin Hamiltonian for an $S=1/2$, $I=3/2$ system with isotropic g is

$$H = g\beta\mathbf{B}\mathbf{S} + g_n\beta_n\mathbf{B}\mathbf{I} + \mathbf{S}\cdot\mathbf{A}\cdot\mathbf{I} + \mathbf{I}\cdot\mathbf{Q}\cdot\mathbf{I}. \quad (1)$$

The hyperfine tensor \mathbf{A} has principal values (A_{xx}, A_{yy}, A_{zz}). In the point-dipole approximations it can be written in the form ($A_{\text{iso}} - T, A_{\text{iso}} - T, A_{\text{iso}} + 2T$) where A_{iso} is the isotropic hyperfine coupling constant and $T = gg_n\beta_n\beta/r^3$, where r is the effective electron-nucleus distance. \mathbf{Q} is the nuclear quadrupole tensor; its components in its principal axes system are $Q_{zz}^P = Q/2I(2I-1)$, $Q_{xx}^P = -Q_{zz}^P(1-\eta)/2$, $Q_{yy}^P = -Q_{zz}^P(1+\eta)/2$, where $\eta = (Q_{xx}^P - Q_{yy}^P)/Q_{zz}^P$ and $Q = e^2qQ_n/h$ is the quadrupole coupling constant due to a quadrupole moment Q_n interacting with the electric-field gradient q at the nucleus. The principal axes systems of the tensors \mathbf{A} and \mathbf{Q} are related by the Euler angles (α, β, γ).³⁶ The spin Hamiltonian (1) in matrix form consists of two blocks, H^α and H^β , corresponding to the α and β electron-spin states, and the expression for the three-pulse stimulated

echo is calculated according to expression (3a).³⁷ In this expression ω_{ij}^α are the nuclear transition frequencies $\omega_i^\alpha - \omega_j^\alpha$ belonging to the α electron-spin manifold and similarly ω_{kn}^β belonging to the β manifold, with the various ω_i^α , ω_i^β being the eigenvalues of the H^α and H^β Hamiltonians, respectively. The eigenvector of the i th eigenstate of the α spin manifold ($m_s = +1/2$) is expressed as

$$\begin{aligned} \psi_i^\alpha = & c_{i,3/2}^\alpha |1/2, +3/2\rangle + c_{i,1/2}^\alpha |1/2, +1/2\rangle \\ & + c_{i,-1/2}^\alpha |1/2, -1/2\rangle + c_{i,-3/2}^\alpha |1/2, -3/2\rangle. \end{aligned}$$

Using the vector \mathbf{C}_i^α which has components of complex numbers $c_{i,3/2}^\alpha$, $c_{i,1/2}^\alpha$, $c_{i,-1/2}^\alpha$, and $c_{i,-3/2}^\alpha$ we construct the matrix elements M_{kn} (Ref. 37)

$$M_{kn} = \mathbf{C}_k^{\alpha+} \mathbf{C}_n^\beta. \quad (2)$$

The matrix element M_{kn} gives the EPR transition amplitude from the k th sublevel within the α spin manifold to the n th sublevel within the β spin manifold. By using these matrix elements the modulation coefficients X_{ij} are calculated for each spin manifold according to Eqs. (3b) and (3c).

$$\begin{aligned} E(\tau+T) = & \frac{1}{(1+2I)} \left\{ \sum_{i,k} |M_{ik}|^4 + \frac{1}{2} \sum_{i \neq j} X_{ij}^\alpha [\cos \omega_{ij}^\alpha \tau + \cos \omega_{ij}^\alpha (\tau+T)] + \frac{1}{2} \sum_{k \neq n} X_{kn}^\beta [\cos \omega_{kn}^\beta \tau + \cos \omega_{kn}^\beta (\tau+T)] \right. \\ & \left. + \sum_{i \neq j} \sum_{k \neq n} X_{ij, kn}^{(\alpha, \beta)} [\cos \omega_{ij}^\alpha (\tau+T) \cos \omega_{kn}^\beta \tau + \cos \omega_{ij}^\alpha \tau \cos \omega_{kn}^\beta (\tau+T)] \right\}, \quad (3a) \end{aligned}$$

$$X_{ij}^\alpha = 2 \sum_k |M_{ik}|^2 |M_{jk}|^2, \quad X_{kn}^\beta = 2 \sum_i |M_{ik}|^2 |M_{in}|^2, \quad (3b)$$

$$X_{ij, kn}^{(\alpha, \beta)} = 2 \operatorname{Re}[M_{ik}^* M_{in} M_{jn}^* M_{jk}]. \quad (3c)$$

Simulation of ESEEM spectra for $I=3/2$: Before we attempt to simulate the experimental spectra we explore the effects of the various parameters of the spin Hamiltonian of the ESEEM spectrum for $I=3/2$ in order to isolate the parameters which determine the main characteristics in the time- and frequency-domain ESEEM spectra. Several approximation methods, involving mainly perturbation theories, have been developed to account for the quadrupole effect on the ESEEM pattern.^{17,38-40} While for $I=1/2$ and $I=1$ systems there is ample experimental and theoretical work in the literature, an analogous basic detailed analysis for the $I=3/2$ is still lacking. Reijerse and Keijzers²⁴ have investigated the dependence of ESEEM powder line shapes for $I=1/2$, 1 and 3/2 on the various coupling parameters. Their work dealt with a single nuclear coupling and only the frequency-domain spectra have been discussed. In the present case we have investigated in detail the properties of the ESEEM spectra for $I=3/2$ in the time and in the frequency domain for single and multiple nuclear coupling. All the ESEEM spectra have been calculated by exact numerical diagonalization of the spin Hamiltonian (1) thus imposing no

restriction on the relative size of the terms in the spin Hamiltonian. In the B_2O_3 glass samples under study, the quadrupole interaction of the ^{11}B ($I=3/2$) nucleus cannot be neglected² and both weak and strong hyperfine couplings occur. Thus in order to extract the maximum information from the spectral analysis both the time- and the frequency-domain spectra have to be analyzed. The calculations have been performed for a nuclear Larmor frequency of ^{11}B nucleus of $\nu_I = 4.8$ MHz. The results may be easily applied to other $I=3/2$ nuclei (^7Li , ^{23}Na) by appropriate scaling of the coupling parameters based on the Larmor frequencies.

$A_{\text{iso}}=0$: For a $A_{\text{iso}}=0$ and $e^2qQ/h=0.5$ MHz the ESEEM spectrum is characterized by a single modulation frequency at ν_I . The introduction of a modest anisotropic hyperfine coupling (T) affects mainly the modulation depth, while the corresponding frequencies remain unchanged. An increased T induces a very slow frequency which is superimposed on the main oscillation at ν_I [trace c , Fig. 1(A)]. In the frequency domain [trace c , Fig. 1(B)], this is manifested as weak sidebands around ν_I . For $e^2qQ/h=2.4$ MHz the peak at ν_I is split and the effect of increased T becomes more

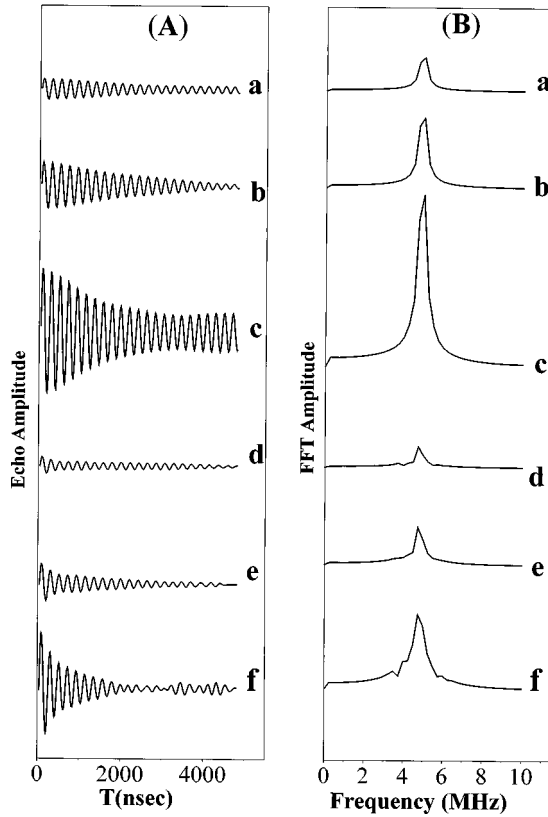


FIG. 1. Calculated three-pulse normalized ESEEM ($\tau=120$ ns, $\nu_I=4.7$ MHz, asymmetry parameter $\eta=0.2$, $A_{\text{iso}}=0$) for a single $I=3/2$ nucleus in the time (A) and frequency domain (B), respectively. The e^2qQ/h values are 0.5 MHz (a, c, d) or 2.4 MHz (b, d, f). The isotropic hyperfine coupling A_{iso} is 0.0 MHz (a, b), 1.0 MHz (c, d), and 5.0 MHz (e, f). In all the cases the axial hyperfine coupling T is 0.05 MHz in (a, d), 0.15 MHz in (b, c) and 0.25 MHz in (c, f).

prominent. Now the slow frequency component attains considerable amplitude and induces a phase inversion in the time-domain signal, see Fig. 1(A) trace f. Thus a concluding observation from Fig. 1(A) is that for $A_{\text{iso}}=0$ a phase inversion requires the existence of both considerable quadrupole coupling and a nonzero anisotropic hyperfine interaction.

$A_{\text{iso}} \neq 0$: For negligible e^2qQ/h , a weak isotropic hyperfine coupling $A_{\text{iso}} \leq 2\nu_I$ splits the frequency-domain ESEEM spectrum into two lines disposed symmetrically around ν_I , see traces c and e in Fig. 2(A).

The influence of increasing e^2qQ/h for various A_{iso} values may also be discussed by referring to Fig. 2. For $A_{\text{iso}}=0$, the quadrupole interaction introduces fine structure in the frequency-domain spectra, see traces a, b in Fig. 2(B). In the time domain this effect is manifested as a faster damping of the modulation in addition to a phase inversion at $\tau \sim 3.2 \mu\text{s}$, see traces a, b in Fig. 2(A). The damping of the modulation and the phase inversion phenomenon due to the quadrupole coupling has been analyzed previously for systems $I=1$ (Refs. 41 and 38) and $5/2$.^{39,40}

For $I=3/2$ there is a total of six nuclear transitions for each spin manifold, three $|\Delta m_I|=1$, two $|\Delta m_I|=2$, and one $|\Delta m_I|=3$. The simulations show that the ESEEM spectral features are determined by the $|\Delta m_I|=1$ transitions with minor contributions from the $|\Delta m_I|=2$. The $|\Delta m_I|=3$ transitions have negligible intensity and their contribution is practically not resolved. The contribution of each modulation

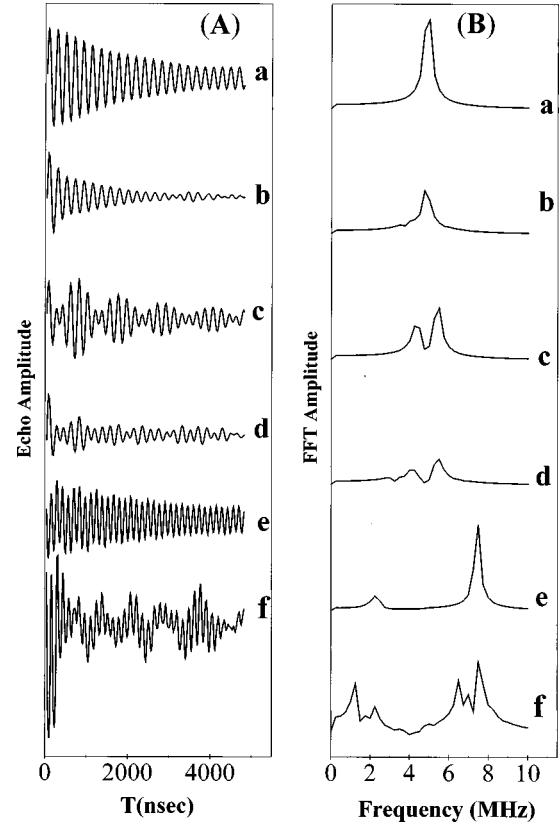


FIG. 2. Calculated three-pulse normalized ESEEM for a single $I=3/2$ nucleus in the time (A) and frequency domain (B), respectively. The e^2qQ/h values are 0.5 MHz (a, c, d) or 2.4 MHz (b, d, f). The isotropic hyperfine coupling A_{iso} is 0.0 MHz (a, b), 1.0 MHz (c, d), and 5.0 MHz (e, f). In all the cases the axial hyperfine coupling T is 0.2 MHz. Other parameters as in Fig. 1.

frequency is determined by the modulation coefficients X_{ij} in Eq. (3). As an illustrative example, the relative contributions of the various $|\Delta m_I|=1, 2$ transitions to the frequency-domain ESEEM spectra for $A_{\text{iso}}=6$ MHz are shown in Fig. 3.

For small e^2qQ/h the three $|\Delta m_I|=1$ transitions have comparable contributions to the ESEEM spectrum, consisting of symmetric spectra split around the Larmor frequency by $A_{\text{iso}}/2$, Fig. 3(B). An increased e^2qQ/h affects the $|m_I=+1/2\rangle \leftrightarrow |m_I=-1/2\rangle$ transition to second order, while all the other $|\Delta m_I|=1$ transitions are broadened to first order.⁴⁰ In the ESEEM spectrum the $|m_I=+1/2\rangle \leftrightarrow |m_I=-1/2\rangle$ features are unperturbed and remain essentially sharp, see Fig. 3(A). The quadrupole coupling disperses all the other nuclear frequencies and concomitantly causes a second-order shift of their center of gravity.⁴⁰ Thus for the case of ¹¹B in B₂O₂ where $e^2qQ/h \sim 2.6-2.8$ MHz, the most prominent features in the experimental ESEEM spectrum should originate from the $|m_I=+1/2\rangle \leftrightarrow |m_I=-1/2\rangle$ transition. The first-order nuclear frequencies are at $\nu_\alpha = \nu_I + A_{\text{iso}}/2$ and $\nu_\beta = \nu_I - A_{\text{iso}}/2$ and thus their frequency difference is to a first approximation a measure of A_{iso} . As it is shown below, in the corresponding HSCORE spectrum these transitions would give rise to two cross peaks at positions (ν_α, ν_β) and (ν_β, ν_α) both in the (+, +) quadrant.

$A_{\text{iso}}=2\nu_I$: In the case of the exact compensation ($A_{\text{iso}}=2\nu_I$) in the $m_s=+1/2$ manifold the effective magnetic

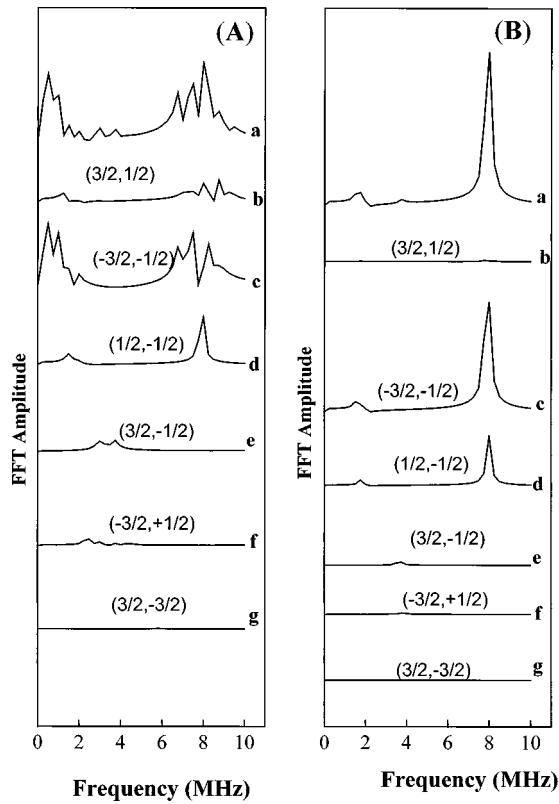


FIG. 3. Calculated three-pulse ESEEM corresponding to $|\Delta m_I| = 1$ (a, b, c), $|\Delta m_I| = 2$ (d, e), and $|\Delta m_I| = 3$ (f) nuclear transitions, for a single $I = 3/2$ nucleus. The $e^2qQ/h = 2.4$ MHz (A) or 0.5 MHz (B). In all the cases $A_{\text{iso}} = 6.0$ MHz, $T = 0.08$ MHz. The top spectrum (a) in each panel is the total spectrum. Other parameters as in Fig. 1.

field which is $B_{\text{eff}} = [v_I - A_{\text{iso}} / (2m_I - 1)]$ is zero and in the presence of a nuclear quadrupole coupling the nuclear transitions are degenerate occurring at a frequency⁴²

$$\nu_c = 6[e^2qQ/4I(2I-1)h](1 + \eta^2/3)^{1/2}. \quad (4)$$

In the other m_s manifold the hyperfine and nuclear Zeeman terms are additive. The $|m_s = -1/2, m_I = +1/2\rangle$ to $|m_s = -1/2, m_I = -1/2\rangle$ transition occurs at a frequency close to $2\nu_I$. In this case a single strong narrow feature dominates the ESEEM spectrum, [Figs. 4(A), 4(B) trace d], while the high frequency component at $2\nu_I$ is barely resolved.

The high-frequency component at $\sim 2\nu_I = 9.6$ MHz is not affected to first order by the e^2qQ/h value. The only effect is that on increased e^2qQ/h values this feature becomes structured. In the presence of, even a small, hyperfine anisotropy the singular feature at ν_c is dispersed and its intensity is strongly diminished.²⁴ Thus in real powder systems with $A_{\text{iso}} = 2\nu_I$ where a small nonzero anisotropy might be always present, it is rather unlikely that the zero-anisotropy strong feature at ν_c will be resolved in the ESEEM spectra. For a pure isotropic hyperfine coupling which deviates from $2\nu_I$, i.e., either $A_{\text{iso}} > 2\nu_I$ or $A_{\text{iso}} < 2\nu_I$, the ESEEM spectra again degrade, Fig. 4, and only weaker low-frequency components are resolved. We notice that for A_{iso} close to $2\nu_I$, in the corresponding HSCORE spectrum the cross peaks are expected at frequencies close to $(\nu_c, 2\nu_I)$.

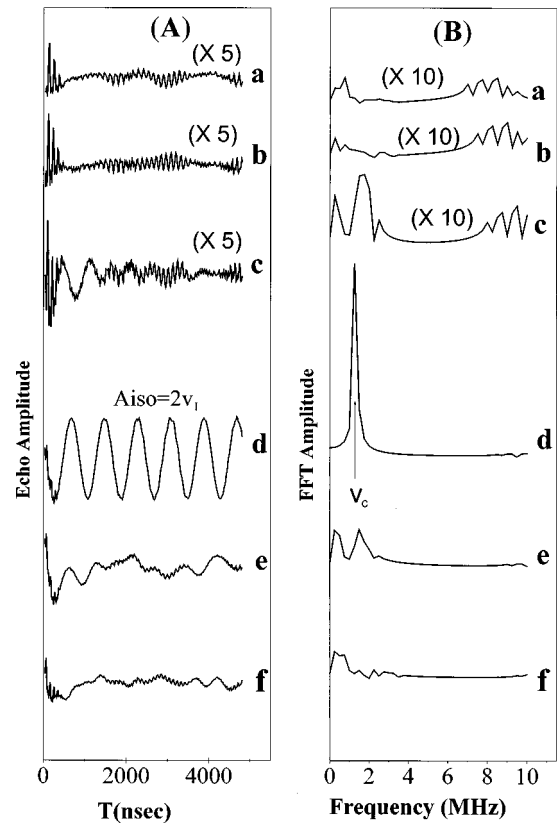


FIG. 4. Effect of A_{iso} on the ESEEM of a single $I = 3/2$ nucleus in the time (A) and frequency (B) domain. A_{iso} is 6.5 MHz (a), 7.5 MHz (b), 8.5 MHz (c), 9.6 MHz $= 2\nu_I$ (d), 10.5 MHz (e), and 11.5 MHz (f). The strong singular feature at ν_c (see text) for the case of the exact cancellation $A_{\text{iso}} = 2\nu_I$ is marked. In all the cases $T = 0.08$ MHz, $e^2qQ/h = 2.4$. Other parameters as in Fig. 1.

Effect of β : So far the preceding discussion concerned $I = 3/2$ ESEEM spectra calculated for collinear quadrupole and hyperfine tensors. In combination with the quadrupole interaction the misalignment between the tensors \mathbf{Q} and \mathbf{A} results in both line-broadening and line shape changes, Fig. 5.

As β approaches 90° the broadening of the lines becomes more severe. Concomitantly the feature $|\Delta m_I| = 2$ at higher frequencies attains considerable intensity, Fig. 5, lower trace. The effect is minimal for the $|m_I = +1/2\rangle \leftrightarrow |m_I = -1/2\rangle$ transition. In general in the presence of quadrupole interaction the intensities of the two major features in the frequency domain are asymmetric. For a positive A_{iso} and $\beta = 0^\circ$ the low frequency is weaker, while the high frequency peak is strong and sharp; this difference becomes more prominent at increased Q values. This asymmetry between these two hyperfine components originates from the different angular dependence of the anisotropic and the quadrupole interaction.⁴⁰ While the sign of the anisotropic hyperfine term is different for the $m_s = +\frac{1}{2}$ and $-\frac{1}{2}$ electron-spin manifolds, the quadrupole terms have the same sign. Depending on the relative signs of the hyperfine and quadrupole terms this may result in excessive broadening of the signals of one manifold and a narrowing of the signals of the other manifold.

Multinuclear ^{11}B couplings: In the case of disordered systems where N nuclei are interacting with the paramagnetic center the total echo pattern calculated using the spherical approximation⁴¹ is

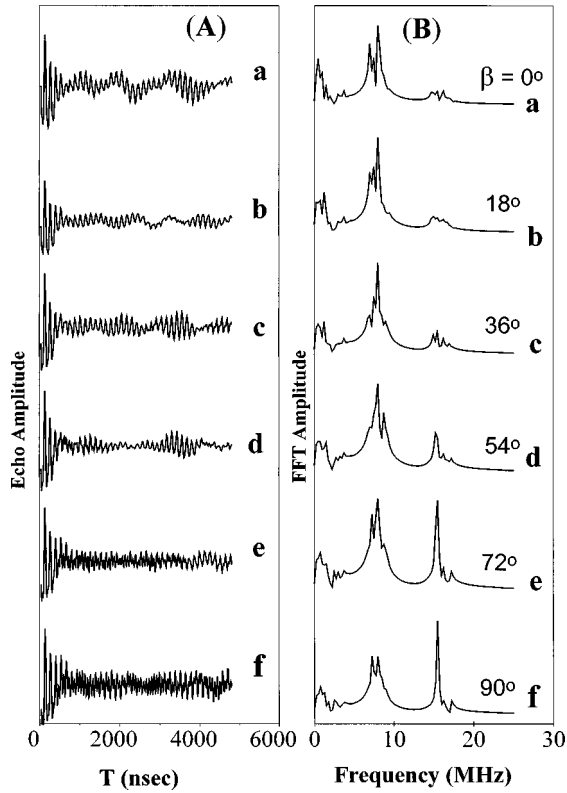


FIG. 5. Effect of the Euler angle β on the ESEEM of a single $I=3/2$ nucleus in the time (A) and frequency (B) domain. $\beta=0^\circ$ (a), 18° (b), 36° (c), 54° (d), 72° (e), and 90° (f). In all the cases $A_{\text{iso}}=6$ MHz, $T=0.08$ MHz, $e^2qQ/h=2.4$. Other parameters as in Fig. 1.

$$\langle E \rangle^N = \left[\left(\frac{1}{4\pi} \right) \int_0^{2\pi} \int_0^\pi E_I(\theta, \phi, r) \sin \theta d\theta d\phi \right]^N. \quad (5)$$

According to the conventional formulation θ and ϕ are the polar and azimuthal angles of the i th nuclear position vector with respect to the external magnetic field.¹⁷ In the spherical approximation any mutual nuclear correlation is ignored and all nuclei are considered to be independently distributed over a sphere of radius r . This approximation has been discussed in detail in the literature^{17,41} mainly for $^2\text{H}(I=1)$ modulation and for $^{27}\text{Al}(I=5/2)$ and it is found to be valid for distant (“matrix”) nuclei^{17,41} for which $A_{\text{iso}} \cong 0$. For the range of matrix boron nuclei in the B₂O₃ glass our calculations show that the spherical model is reliable for effective distances ≥ 3.8 Å.

The effect of multiple nuclear ($I=3/2$) coupling for the case of $A_{\text{iso}}=0$ is examined in Fig. 6 for a quadrupole interaction of either 0.5 MHz (traces a, b, c) or 2.4 MHz (traces d, e, f).

When compared with a single nucleus (traces a, d), multiple equivalent nuclei result in an increase of the modulation depth in the time domain or the intensity of the peaks in the frequency domain. For small number of nuclei, $N < 8$, practically no new features are generated due to the multiple nuclear coupling; at large N a broad, weak, “combination” feature at frequency $\sim 2\nu_I$ emerges. It is interesting to notice that in the case of the cancellation condition ($A_{\text{iso}}=2\nu_I$), the multiple nuclear coupling induces new features at frequency

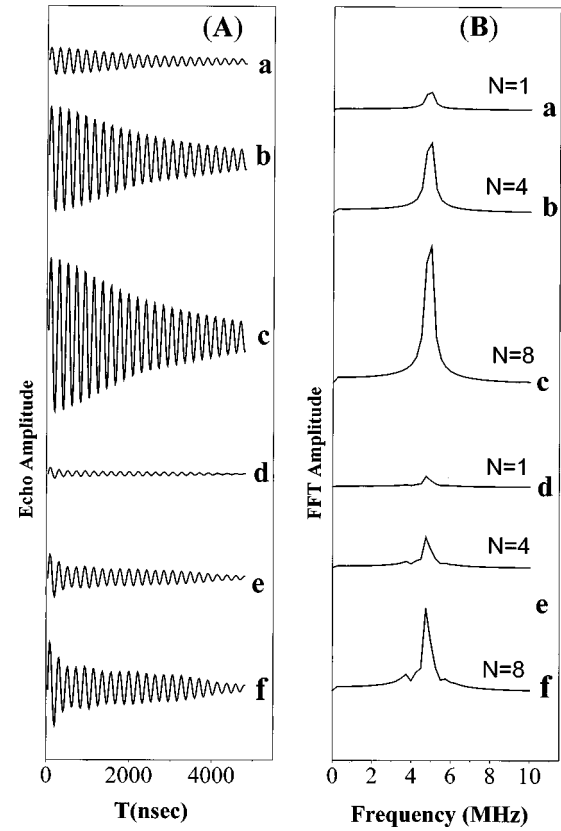


FIG. 6. Calculated three-pulse normalized ESEEM calculated according to the spherical model for $N=1$ (a, d), 4 (b, e), 8 (c, f) nuclei with $I=3/2$ in the time (A) and frequency domain (B), respectively. The e^2qQ/h values are 0.5 MHz (a, b, c) or 2.4 MHz (d, e, f, g). In all the cases $A_{\text{iso}}=0$ MHz, $T=0.08$ MHz. Other parameters as in Fig. 1.

positions which are harmonics of the single frequency ν_c , i.e., at frequencies $2\nu_c, 3\nu_c, 4\nu_c, \dots$, see Fig. 7. By inspecting Fig. 7 the following practical rule is deduced: for N equivalent nuclei coupled to the electron spin a number of k combination peaks is expected where the algorithm $N = 2^{k-1}$ is obeyed.

¹⁰B($I=3$) ESEEM: The natural abundance of the ¹⁰B nuclei ($I=3$, $\nu_I=1.6$ MHz at 3.5 mT) is 19.8% and thus it is of relevance to examine their contribution in the ESEEM spectra in B₂O₃ glass. In B₂O₃ glass, ¹⁰B nuclei are characterized by relatively large quadrupole coupling constants ~ 5.6 MHz (Ref. 2) and this renders the ¹⁰B quadrupole interaction dominant in the ¹⁰B nuclear spin Hamiltonian. Due to the angular dependence of the quadrupole interaction the ¹⁰B nuclear transitions are strongly dispersed. Typical stimulated-echo ESEEM spectra for various A_{iso} values are presented in Fig. 8.

The spectra are characterized by low-frequency modulations which in the frequency domain correspond to complex overlapping features around ν_1 . In real systems, where the more abundant ¹¹B nuclei (80.2%) might have nuclear frequencies which overlap with those due to ¹⁰B, it is rather unlikely that the ¹⁰B spectra could be resolved. Thus in the B₂O₃ glass, we rely exclusively on the ¹¹B($I=3/2$) ESEEM spectra for the estimation of the spin Hamiltonian parameters.

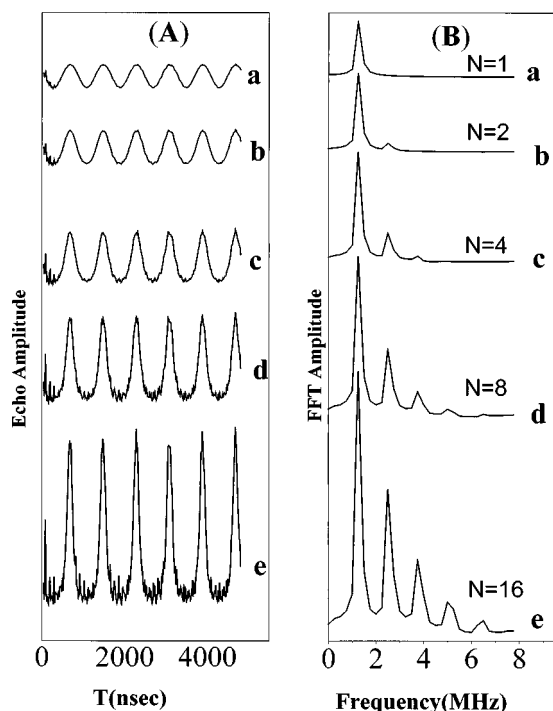


FIG. 7. Calculated three-pulse normalized ESEEM calculated according to the spherical model for $N=1$ (a), 2 (b), 4 (c), 8 (d), 16 (e) nuclei with $I=3/2$ for $A_{\text{iso}}=2\nu_I$. In all the cases $e^2qQ/h=2.4$ MHz, $T=0.08$ MHz. Other parameters as in Fig. 1.

RESULTS

CW EPR measurements: The c.w. EPR spectrum of a γ -irradiated B_2O_3 glass and crystal are shown in Figs. 9(A) and 9(B), respectively. The c.w. EPR spectrum, consists of five-lines plus a shoulder, the outer features differing by ~ 50 G. In the crystalline sample, the c.w. EPR spectrum [Fig. 9(B)] has the same structure with fairly minor differences. Noticeably, the low-field broad shoulder of the glass sample [in Fig. 9(A)] is present in the spectrum of the crystalline sample [Fig. 9(B)], too.

Stimulated-echo ESEEM in B_2O_3 glass: Figure 10(A) shows the time-domain ESEEM for B_2O_3 glass. In order to avoid missing modulation frequencies due to τ -suppression effects,¹⁷ the echo decay was recorded at several τ values.

The ESEEM spectra have been recorded at the maximum intensity of the echo-detected field-swept spectrum which is displayed in the inset of Fig. 10(A). The ESEEM traces are dominated by modulation components with periods of about 550 and 260 ns; at certain τ values weaker components are resolved. The frequency-domain spectra obtained after fast Fourier transform (FFT) of the time-domain data for a series of τ -values are depicted in Fig. 10(B). The spectra are dominated by features centered at 1.6 and 4.8 MHz and these correspond to the strong modulations observed in the time-domain spectra in Fig. 10(A). Additional weaker peaks disposed symmetrically around the 4.8 MHz peak are resolved at certain τ values. The 1.6 MHz feature is broad and structured. We notice the total absence of peak at the ^1H -Larmor frequency at ~ 15 MHz which would originate from weakly coupled protons¹⁷ in the glass network. No other peaks are detected at higher frequencies.

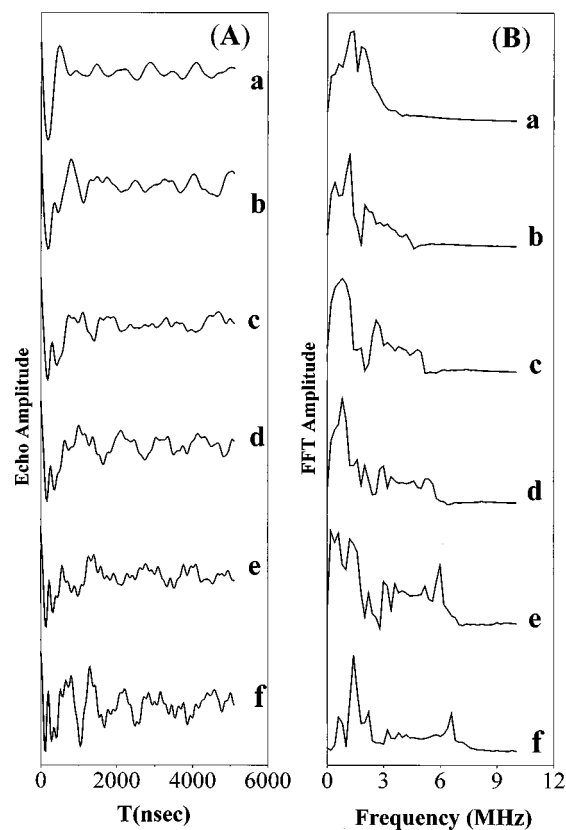


FIG. 8. Calculated three-pulse normalized ESEEM of a single ^{10}B ($I=3$, $\nu_I=1.6$ MHz) nucleus in the time (A) and frequency (B) domain. A_{iso} is 0.5 MHz (a), 1.0 MHz (b), 2.0 MHz (c), 4.0 MHz (d), 6.0 MHz (e), and 8.0 MHz (f). In all the cases $T=0.1$ MHz, $e^2qQ/h=5.6$ MHz, $\eta=0$.

In principle the observed peaks in Fig. 10(B) arise from nuclear spins in the vicinity of the paramagnetic center interacting with the electron spin.^{16–18} In the B_2O_3 sample, the ^{11}B ($I=3/2$, natural abundance 80.2%) and ^{10}B ($I=3$, natural abundance 19.8%) are the only atoms having non-zero nuclear spins. The main peaks at 1.6 and 4.8 MHz are near the Larmor frequencies of the ^{10}B and ^{11}B nuclei, respectively. The magnetic interactions which determine the observed ESEEM depend on the details of the electron-nucleus mutual disposition and this in turn reflects the local structure of the paramagnetic centers in the sample.

In order to facilitate the assignment of the observed peaks, we performed 2D-HYSCORE experiments^{19,20} in order to identify the correlated peaks originating from the same nucleus. In addition, the 2D-HYSCORE experiment can unravel modulations which are not well resolved in the stimulated 1D-ESEEM spectrum.²³

2D-HYSCORE: The 2D-HYSCORE experiment, like the 1D stimulated ESEEM, suffers from the τ -suppression effect.^{19,20,23} If one of the two conjugated nuclear transitions is suppressed then in the 2D-HYSCORE spectrum in the frequency domain the corresponding correlation peak has diminished amplitude. Therefore, we have performed several 2D-HYSCORE experiments employing a series of different τ intervals between the first two pulses in the four-pulse sequence. Representative contour plots of a 2D-HYSCORE spectra recorded for $\tau=248$ and 168 ns for B_2O_3 glass is displayed in Fig. 11. The features on the diagonal or parallel

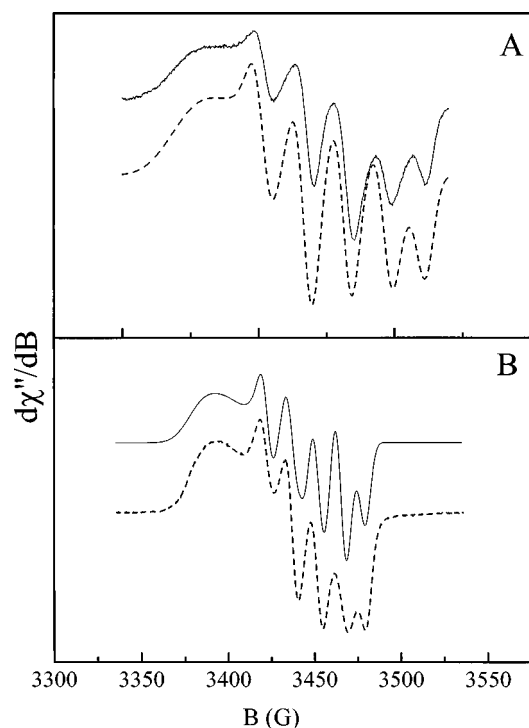


FIG. 9. Experimental c.w. X-band EPR spectra (solid lines) of the B₂O₃ glass (A) and crystal (B). The dashed lines are simulated spectra by using the parameters listed in Table I.

to the frequency axes are mainly experimental artefacts due to imperfections of the pi pulse and the phase cycling,^{19,35} and should be ignored.

In the (+,+) quadrant of the 2D-HYSCORE for $\tau = 248$ ns in Fig. 11, two sets of symmetric cross peaks, marked by the dashed lines, are resolved; since they are symmetric with respect to the diagonal, we will refer to only one of the two halves. Their frequency positions are (1.9, 7.2 MHz) and (3.5, 5.6 MHz). In the 1D-ESEEM spectrum, Fig. 10(B), these features are vaguely resolved. At $\tau = 168$ ns the outer cross peaks at (1.9, 7.2 MHz) are even better resolved, while the (3.7, 5.8 MHz) cross peaks are suppressed. Now an additional feature is resolved in the (+,+) quadrant and this is perpendicular to the diagonal, marked by the inner dashed rectangle in the $\tau = 168$ ns panel of Fig. 11. All the observed cross peaks are located on a line perpendicular to the diagonal passing through the point (4.8, 4.8 MHz), which is the ¹¹B-Larmor frequency (ν_l) at this magnetic field. Based on this, we assign these cross peaks to ¹¹B nuclear spins in the vicinity of the paramagnetic oxygen.

The HYSCORE spectrum contains also a strong feature on the diagonal at (1.6, 1.6 MHz), i.e., the ¹⁰B-Larmor frequency. At $\tau = 248$ ns a continuum of cross peaks close to the (1.6, 1.6 MHz) cross peak, are resolved, and these are severely suppressed at $\tau = 168$ ns. In the case of ¹⁰B, the nuclear quadrupole interaction is expected to be stronger than the Larmor frequency.²⁻⁴ The numerical simulations (Fig. 8) show that in the case of for all the used ¹⁰B-hyperfine interactions, the quadrupole coupling broadens the spectral lines. Only features around the ¹⁰B-Larmor frequency are resolved. In the 2D-HYSCORE these result in overlapping features at the low frequency part of the (+, -) quadrant and this is the origin of the agglomerate that is

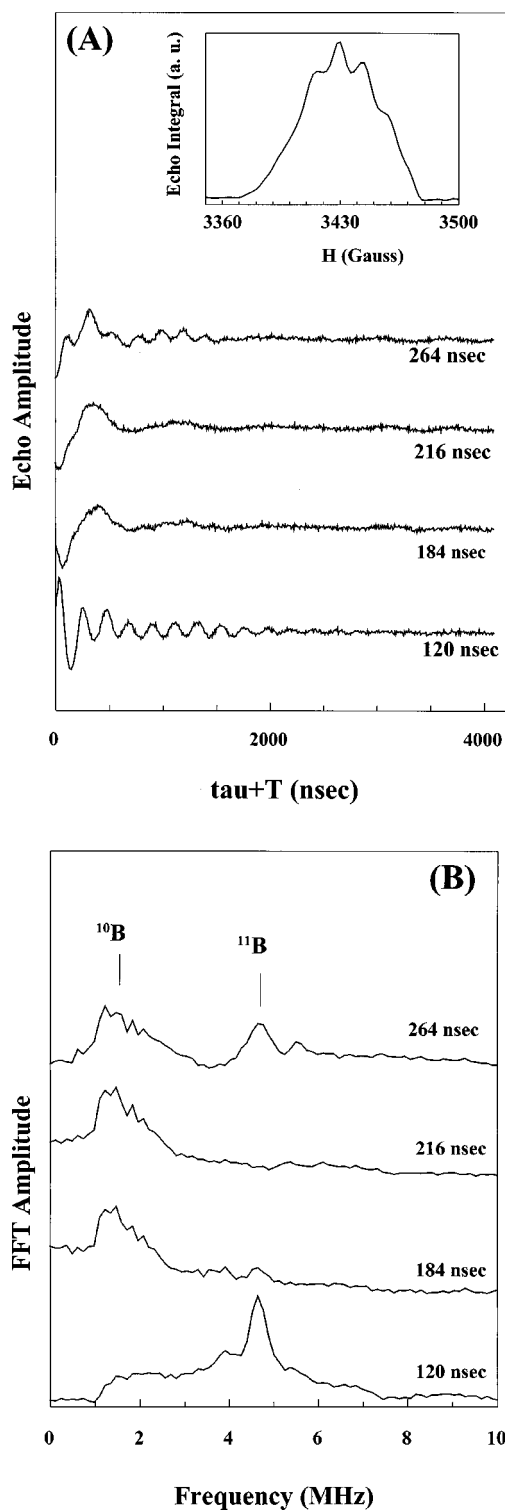


FIG. 10. (A) Experimental three-pulse ESEEM spectra of B₂O₃ glass recorded at the indicated τ values, i.e., the time between the first and the second microwave pulses. *Inset*: Integral of the electron spin echo of B₂O₃ glass resulting from a two-pulse sequence, as a function of the magnetic field. (B) Fast-Fourier transform of the spectra in (A). Experimental conditions: microwave frequency, 9.68 GHz; magnetic-field strength 3540 G; sample temperature 8 K; time interval between successive pulse sets, 1 ms; 800 events were averaged at each time point. For each τ value 512 points were collected at 8 ns intervals; a four-step phase cycling was employed.

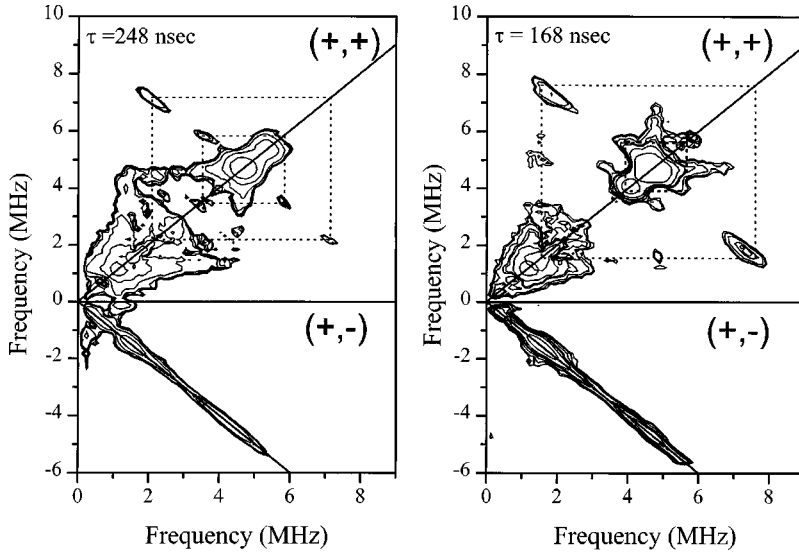


FIG. 11. Experimental 2D-HYSCORE spectrum (contour plots) of B_2O_3 glass recorded at $\tau = 168$ ns. Experimental conditions: $t_1 \times t_2 = 256 \times 256$ points; start values $t_1 = 40$ ns, $t_2 = 120$ ns; other conditions as in Fig. 10.

observed around (1.6, 1.6 MHz) in Fig. 11, arising from ^{10}B nuclei. Due to their complicated nature the ^{10}B modulations are not suited for further analysis. Thus in the 1D- as well and in the 2D-ESEEM we rely exclusively on the ^{11}B modulations for the evaluation of the coupling parameters.

According to the theoretical analysis for $e^2qQ/h < A_{iso}$, $< 2\nu_I$, the stimulated ^{11}B -ESEEM spectrum is characterized by two features at frequencies $\nu_I \pm A_{iso}/2$ to first order. In the corresponding 2D-HYSCORE spectrum, correlation peaks with frequency coordinates $(\nu_I \pm A_{iso}/2, \nu_I \mp A_{iso}/2)$ are expected. The HYSCORE spectrum is sensitive to the relative signs of the nuclear frequencies; a correlation peak at $(\nu_{ij}^{(\alpha)}, \nu_{mn}^{(\beta)})$ appears in the (+,+) quadrant while the correlation peak $(\nu_{ij}^{(\alpha)}, -\nu_{mn}^{(\beta)})$ appears in the (+,-) quadrant. The relative intensities of the cross peaks at $(\nu_{ij}^{(\alpha)}, \nu_{mn}^{(\beta)})$ and $(\nu_{ij}^{(\alpha)}, -\nu_{mn}^{(\beta)})$ depend on the factors $M_{im} M_{jn}^*$ and $M_{jm} M_{in}^*$, respectively,^{20,37} where the matrix elements of M are calculated according to expression (2). In general, these relative intensity factors differ since they are determined by the matrix elements describing the four possible transitions between the two levels i and j , and m and n in each manifold. Due to this, the two cross peaks having the same absolute frequency values, but being at opposite quadrants, have different intensities. For the transitions $|m_I = +1/2\rangle \Leftrightarrow |m_I = -1/2\rangle$ which are the most intense in our case, if we assign the states i, j to $m_I = +1/2, -1/2$ in the (α) spin manifold and the states m, n to $m_I = +1/2, -1/2$ in the (β) manifold, respectively, the picture is as follows: In the limit of weak hyperfine coupling ($A_{iso} \ll \nu_I$) the matrix elements $M_{im} = M_{+1/2, +1/2}$ and $M_{jn}^* = M_{-1/2, -1/2}^*$ are strong since they connect two strongly “allowed” EPR transitions, while the $M_{jm} = M_{+1/2, -1/2}$ and

$M_{in}^* = M_{-1/2, +1/2}^*$ are negligible since they connect two strongly “forbidden” EPR transitions. Thus the corresponding cross peak at $(\nu_{ij}^{(\alpha)}, \nu_{mn}^{(\beta)})$ in the (+,+) quadrant attains maximal intensity relative to the cross peak at $(\nu_{ij}^{(\alpha)}, -\nu_{mn}^{(\beta)})$ which has minimal intensity. In the opposite limit of strong hyperfine coupling ($A_{iso} \gg \nu_I$), the states m, n in the (β) manifold are labeled as $m_I = -1/2, +1/2$ and by proceeding on the same lines as before we conclude that now it is the cross peak in the (+,-) quadrant which has maximum intensity while the cross peak in the (+,+) quadrant is minimized. Analogous arguments are valid for the intensities of the cross peaks for the other nuclear transitions. In intermediate hyperfine couplings the eigenfunctions have mixed m_I character; in the limiting case of the “exact cancellation” $A_{iso} = 2\nu_I$ the peaks in both the (+,+) and (+,-) quadrants have comparable intensity. This analysis shows that for a $I = 3/2$ nuclear spin with relatively weak hyperfine and quadrupole coupling, the 2D-HYSCORE spectrum is dominated by the $|m_I = +1/2\rangle \Leftrightarrow |m_I = -1/2\rangle$ transition and has to a good approximation the characteristics of an effective $I = 1/2$ system.^{19,20,40}

In the 2D-HYSCORE spectra for B_2O_3 displayed in Fig. 11, the cross peaks are observed in the (+,+) quadrant and according to the previous analysis they correspond to weak hyperfine couplings. Based on the frequency coordinates of their centers a first-order estimation for the corresponding hyperfine couplings gives A_{iso} values of 6 and 2 MHz, respectively. The features centered at (4.7, 4.7 MHz) are due to weakly coupled ($A_{iso} \sim 0$ MHz) “matrix” ^{11}B nuclei; according to the spin-density calculations that we discuss in the following, these are distant borons bearing negligible spin

TABLE I. Spectroscopic parameters of spectrum of the B_2O_3 glass derived from simulation Errors: g values ± 0.0002 , hyperfine coupling ± 0.05 MHz.

CW EPR	g_1	g_2	g_3	A_1 (MHz)	A_2 (MHz)	A_3 (MHz)	LW (G)	A_{iso} (MHz)
B_2O_3 glass	2.0025	2.0118	2.0370	39.44	43.45	22.00	10.0	34.96
B_2O_3 crystal	2.0000	2.0107	2.0415	20.44	40.00	32.00	10.0	30.81

TABLE II. g values and normalized isotropic hyperfine coupling constants $\langle A \rangle / A_s$ of oxygen-related centers observed in a number of glasses (taken from Ref. 12).

Material	Nucleus	g_1	g_2	g_3	$\langle A \rangle / A_s$
Silicate glass	²⁹ Si	2.003	2.009	2.019	0.010
Titanate glass	^{47,49} Ti	2.003	2.010	2.022	
Germanate glass	³⁷ Ge	2.002	2.008	2.051	
Phosphate glass	³¹ P		2.010		0.009
Aluminate glass	²⁷ Al		2.009		0.005
Niobate glass	⁹³ Nb		2.01		0.002
Borate glass	¹¹ B	2.002	2.010	2.035	0.013

density. We point out the enhanced resolution of the HYSCORE experiment compared to the 1D stimulated ESEEM and this has been discussed previously;²³ for example, in the case of the cross peaks in Fig. 11, the corresponding peaks in the 1D-ESEEM spectra, Fig. 10(B), are barely resolved.

CW EPR Spectra Simulations: Figure 9(A) (dashed line) shows the calculated EPR spectrum of the B₂O₃ glass. Table I gives the spectroscopic parameters that were used for the simulation.

Figure 9(B) (dashed line) shows the simulated EPR spectrum of the B₂O₃ crystal. The best fit was done with the parameters given in Table I. The A_{iso} values were calculated by the relation $A_{\text{iso}} = (A_1 + A_2 + A_3)/3$.

Table II summarizes the g values observed in a number of glasses and attributed to nonbridging oxygen.¹² This table serves as a comparison with our g values derived from the simulation of the spectra of the B₂O₃ glass and crystal.

MO Calculations: The MNDO method is very well suited for optimizing the geometry of the local structure of a particular unit. This method was used first to optimize the structure of boroxol units and obtain a quick estimate of the spin densities of the various structural units. The optimized geometry was inserted into the GAUSSIAN 94 program so to minimize the CPU time of the calculations. The GAUSSIAN 94 program was also left to optimize the inserted structure.

We started the calculations using a simple HOB(O)₂H₂ triangular unit. Table III gives the most important results for discussion using the MNDO procedure.

The ground state of the HOB(O)₂H₂ triangular unit is given by the wave function:

$$\psi = (0.9533)|p_{z0(2)}\rangle + (0.2959)|p_{zB(3)}\rangle - (0.0435)|p_{z0(4)}\rangle - (0.0409)|p_{z0(5)}\rangle.$$

The other coefficients were zero and left out.

Table III includes also the GAUSSIAN 94 results of the optimization of the same unit. It is evident from this comparison, that the agreement in terms of the geometry optimization between the two methods is excellent. The calculation was continued by removing a hydrogen to allow the unpaired electron to occupy the nonbridging oxygen of the *OBO₂H₂ structural unit. The spin-density calculation of the MNDO method gives a localization of the unpaired electron on the oxygen P_y orbital of about 91%. The B3LYP/6-311G SCF HF spin-density calculations, which are listed also in Table III, give for the boron atom next to the nonbridging oxygen an $A_{\text{iso(SCF-HF)}} = -0.025\ 662$ a.u. that translates into -36.79 MHz. The negative sign indicates that the A_{iso} is due to spin density from spin polarization. The absolute values of this $A_{\text{iso(SCF-HF)}}$ is close to the experimentally determined value of $A_{\text{iso(EXP)}} = 34.96$ MHz.

In a B₂O₃ crystal two crystallographically distinct BO₃ triangles exist with the bond distances and angles given in Table IV. Assuming that one of the oxygen atoms in the triangle is dangling, then we calculate the spin densities summarized in Table IV. We can observe from this comparison that the resulting spin densities between the two distinguishable structures in the crystal are different. The other possible structural arrangements were not considered in this work, recognizing that they will result in different values of spin densities due to the difference in bond angle and distances of oxygen to the central atom.

Figure 12(C) shows a MNDO optimized structure consisting of a boroxol ring with three terminating B(OH)₂ units. A hydrogen was removed from this structure and the remaining atoms with their optimized $\{x, y, z\}$ values were inserted in the GAUSSIAN 94 program for further structural optimization and determination of the A_{iso} parameters. The theoretical spin densities for each atom are given in brackets for each structure in Fig. 12. The calculation gives an A_{iso} value

TABLE III. Structure of a B(OH)₃ unit optimized by either MNDO or GAUSSIAN 94.

	MNDO				GAUSSIAN 94 (B3LYP/6-311 G)			Isotropic hyperfine couplings (MHz)
	Atom type	Bond length ^a	Bond angle ^b	Twist angle ^b	Bond length ^a	Bond angle ^b	Twist angle ^b	
1	H							3.18
2	O	0.9454			0.9656			8.24
3	B	1.3648	115.96		1.3676	117.33		36.80
4	O	1.3723	115.24	179.99	1.3747	116.83	179.99	3.25
5	O	1.3800	118.88	0.00	1.3872	117.62	0.00	33.50
6	H	0.9437	116.59	180.00	0.9629	122.68	-179.99	31.81
7	H	0.9427	117.51	179.99	0.9636	123.08	179.99	

^aangstroms (Å).

^bdegrees.

TABLE IV. Electronic configuration for two distinct triangles, given in Ref. 11, for B_2O_3 crystal calculated by GAUSSIAN 94 (B3LYP/6-311 G).

	Atom Type	Bond length ^b	Bond angle ^c	Twist angle ^c	Spin densities at each atomic orbital ^a				
					<i>S</i>	<i>P_x</i>	<i>P_y</i>	<i>P_z</i>	Total
1	H				0.48	0.00	0.00	0.00	000.48
2	O	0.9467			0.16	0.33	045.28	0.00	047.76
3	B	1.3840	114.33		0.11	0.00	000.55	0.00	000.66
4	O	1.4010	113.80	-0.01	0.16	82.38	010.94	0.00	093.48
5	O	1.3360	124.60	180.03	0.11	52.11	807.13	0.00	859.36
6	H	0.9437	117.04	-179.91	0.25	0.00	0.00	0.00	000.25
1	H				0.98	0.00	0.00	0.00	000.98
2	O	0.9466			0.50	0.61	030.64	0.00	031.75
3	B	1.3613	115.75		0.10	0.00	001.16	0.00	001.26
4	O	1.3644	121.82	-0.24	0.30	41.58	013.13	0.00	055.00
5	O	1.3875	115.84	180.06	0.08	0.13	909.34	0.01	910.78
6	H	0.9444	117.34	-179.35	0.02	0.00	0.00	0.00	000.23

^a $\times 10^{-3}$.

^bAngstroms (\AA).

^cDegrees.

equal to -31.6989 MHz for the B atom next to the nonbridging oxygen (NBO). The A_{iso} values for the other B atoms are 6.5674, 0.1591, and 0.0201 MHz.

In the next calculation, a $B(OH)_2$ unit was removed from the [Boroxol]-3[B(OH)₂] forming the *NBO-BOROXOL-2[B(OH)₂] structure, Fig. 12(A). Table V gives the results of the GAUSSIAN 94 calculation.

The A_{iso} for the B atom next to the NBO is -33.4794 MHz. The other B atoms within the boroxol rings have A_{iso} values of 6.2234 and 5.9352 MHz. The B atoms of the $B(OH)_2$ units outside the ring have A_{iso} values of 0.3240 and 0.1634 MHz.

The last possibility is another unit consisting of *OB00 connected over the bridging oxygens to two boroxol rings [2OH]-[BOROXOL]-[O-BO*-O]-[BOROXOL]-[2OH]. Fig-

ure 12(B) shows the result of an optimization that helps the reader to visualize this unit. Table V gives the results of A_{iso} values for the different B atoms. The calculation for the B atom next to the NBO gives $A_{\text{iso}} = -34.4729$ MHz. The other A_{iso} values for the B atoms within the boroxol ring closest to the triangle are -1.9082 and -1.9024 MHz. The other B atoms of the ring have A_{iso} less than 1 MHz.

The common electronic configuration for the various structural units in B_2O_3 glass is that the ^{11}B neighbor is in a nodal plane of the unpaired oxygen p_π orbital, so that there is zero overlap between it and the ^{11}B atom core and, consequently, no direct transferred positive hyperfine interaction. The molecular orbital (MO) calculations for the various structural units in B_2O_3 glass predict an unpaired spin density of 0.1% at the boron nucleus. This corresponds to a $A_{\text{iso}} = -31$ to -34 MHz and all these values are rather close to the experimental value estimated by c.w. EPR. A general observation is that for all the studied structural units the MO calculations predict that a spin-polarization mechanism induces a negative isotropic hyperfine coupling for the boron next to the paramagnetic oxygen. For the borons located three bonds away from the paramagnetic oxygen the spin densities are predicted to be positive for the units A and C and negative for the unit C.

DISCUSSION

The c.w.-EPR spectra in $(100-x)$ mole % B_2O_3 x mole % MO ($M = \text{Li, Na, K}$) glasses for $x < 25$ are dominated by centers exhibiting a "five-line-plus-a-shoulder" spectrum with spectroscopic values given in Table II. The same spectrum is obtained for B_2O_3 glasses and a B_2O_3 crystal. The characteristic EPR spectrum, shown in Fig. 9(A), is considered to originate from the hyperfine interaction of the electron spin with one boron nucleus.¹³ However, whether the interacting boron is three or four coordinated is not definitively clarified.¹³⁻¹⁵ Evidence from IR, Raman,⁷⁻⁹ neutron diffraction,⁵ NMR,^{2,3} and previous SCF-HF (Ref. 43) data

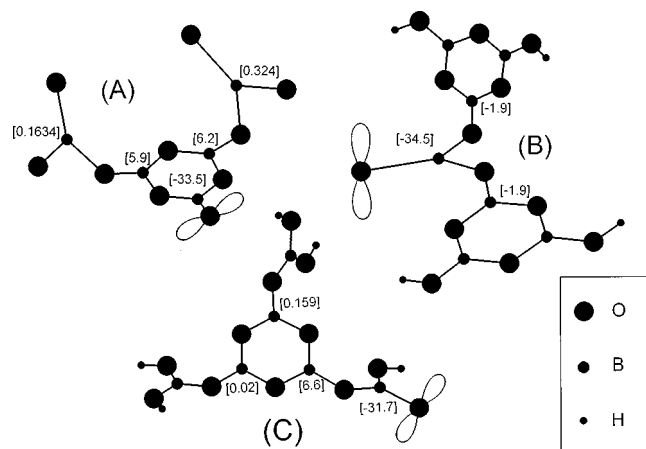


FIG. 12. MNDO optimized structures for the B_2O_3 glass. The oxygen, boron, and hydrogen atoms are illustrated by the large-, middle- and small-size filled circles, respectively. The numbers in the brackets are the isotropic hyperfine couplings (in MHz) at the corresponding atoms calculated by the GAUSSIAN 94 program (B3LYP/6-311 G SCF-HF). The paramagnetic electron localized on the nonbridging oxygen is schematically depicted by the pi-lobe.

TABLE V. Calculated (GAUSSIAN94-B3LYP/6-311 G) isotropic hyperfine coupling parameters (the values for the boron atoms refer to ¹¹B) for three boron-oxygen structural units.

	[Boroxol]-2[B(OH)2]-[BOH-O(NBO)] (Unit C)		[NBO-Boroxol]-2[B(OH)2] (Unit A)		[2OH]-[Boroxol]-[O(NBO)-BOO]-[Boroxol]-2[OH] (Unit B)	
	Atom type	A _{iso} (MHz)	Atom type	A _{iso} (MHz)	Atom type	A _{iso} (MHz)
1	O	-0.0254	O	-26.1043	O	-23.8638
2	B	0.0201	B	5.9352	B	34.4729
3	O	0.0048	O	0.1721	O	-0.9767
4	B	0.1591	B	6.2234	O	-0.4411
5	O	-0.7440	O	-24.0716	B	-1.9082
6	B	6.5674	B	-33.4794	O	-0.9434
7	O	-0.0121	O	-1.0863	O	0.4453
8	O	-0.0145	O	-0.6144	B	-0.0029
9	O	-31.2119	O	-25.9329	B	-0.1075
10	B	0.0043	B	0.3240	O	0.0012
11	B	0.0000	B	0.1634	O	0.0024
12	B	-31.6989	O	-0.0086	O	0.0036
13	O	0.0000	O	0.0206	H	-0.0089
14	O	7.9437	O	-0.0236	H	0.0000
15	O	-0.0030	O	-0.0812	B	-1.9024
16	O	0.0000	H	0.0045	O	-0.9343
17	O	0.0000	H	0.0134	O	0.4568
18	O	0.0000	H	-0.0313	B	-0.0057
19	O	0.0000	H	-0.0067	B	-0.1104
20	H	0.0000			O	0.0030
21	H	-0.0003			O	0.0030
22	H	0.0000			O	-0.0036
23	H	0.0000			H	0.0089

strongly indicate that in B₂O₃ glasses and B₂O₃ crystals that fourfold coordination is absent.

The g values of the centers in B₂O₃ glasses and B₂O₃ crystal that we report in Table I are, within the errors of measurements, the same to those reported for a large number of *nonbridging* oxygens in a variety of glasses, summarized in Table II. Thus, one may suggest that the unpaired electron is trapped by a *nonbridging* oxygen in a threefold-coordinated boron triangle. This statement is reinforced by the present theoretical calculations.

An interesting finding of the calculations is that for all the tested nonbridging oxygens in trigonal structures the calculated A_{iso} is close to the experimentally observed value according to the c.w.-EPR data. This implies that for this boron-oxygen hyperfine interaction the structural details of the units attached next to this interacting boron seem to play only marginal role. In all the cases the unpaired electron is distributed asymmetrically amongst the oxygen's $s(1\%)$, $p_x(2\%)$, $p_y(91\%)$, and $p_z(4\%)$ orbitals.

Structural models for the local boron environment in B₂O₃ glass: According to the experimental 1D-ESEEM and 2D-HYSCORE spectra three types of hyperfine couplings, namely A_{iso} of 6, 2, and <1 MHz are present in the B₂O₃ glass. The molecular-orbital calculations show that a coupling close to 6 MHz is predicted for the borons on the boroxol rings in the structures A and C, while a coupling

close to 2 MHz is predicted for the structure B only, Fig. 12. For all three structural units the $A_{\text{iso}} < 1$ MHz is predicted for the more distant ¹¹B nuclei. Overall the data from the experimental c.w. EPR, 1D-ESEEM and 2D-HYSCORE spectra are consistent with the theoretical calculations based on the three structural units in B₂O₃ glass. Based on the hyperfine couplings calculated for these structural units we proceed in a more detailed analysis of the ESEEM spectra. In the calculations the anisotropic hyperfine coupling T was set equal to the value estimated from the boron-oxygen distance in each unit, according to the point-dipole approximation.

For the case of weak hyperfine couplings it is considered that the time-domain ESEEM spectrum allows a more accurate evaluation of the coupling parameters.⁴⁴ On the other hand, the 2D-HYSCORE reveals that in the irradiated B₂O₃, modulations due to both strongly coupled (with $A_{\text{iso}} < 2\nu_I$) as well as matrix ($A_{\text{iso}} \sim 0$) boron nuclei exist. Thus, it is necessary to analyze the spectra based on both the time- and the frequency-domain spectra. The analysis of the ¹¹B ($I = 3/2$) modulations requires the nuclear quadrupole coupling to be taken into account. In borate glasses, NMR work by Bray and his co-workers revealed that the ¹¹B quadrupole coupling constant e^2qQ/h is sensitive to the coordination geometry of ¹¹B. In fourfold (BO₄) coordinated ¹¹B, the e^2qQ/h is negligible,² while in trigonal coordination (B₂O₃) the quadrupole coupling constant attains a considerable value

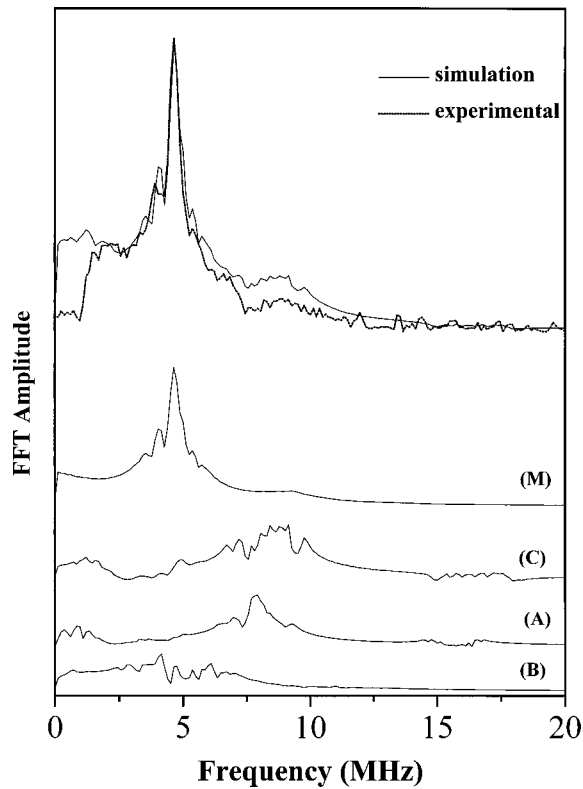


FIG. 13. (Solid lines): Frequency-domain ^{11}B -ESEEM spectra ($\tau = 120$ ns) calculated by using the theoretical ^{11}B nuclear hyperfine couplings for the corresponding structures A (spectrum A), B (spectrum B), and C (spectrum C) in Fig. 12. The spectrum M is the ESEEM spectrum from the matrix ^{11}B nuclei and corresponds to the FFT of the calculated time-domain spectrum in the lower panel in Fig. 14. The top spectrum is the spectrum generated by adding the spectra A, B, C, and M after having been scaled by 0.9, 0, 0.2, and 1.0, respectively. (Dotted line): the experimental ESEEM spectrum [taken from Fig. 10(B) for $\tau = 120$ ns] is superimposed for comparison.

2.6–2.8 MHz.³ Noticeably the NMR work on crystalline B_2O_3 showed that the e^2qQ/h is 2.7 MHz,¹⁰ which suggests a trigonal geometry and this is in accordance with the x-ray data which show in crystalline B_2O_3 all of the boron atoms are in trigonal units.¹¹ Thus in both vitreous and crystalline B_2O_3 where there are only threefold-coordinated borons^{1–11} the e^2qQ/h value is expected to be of the order of 2.6–2.7 MHz. The numerical simulations that we discuss in the following show that for hyperfine couplings of 2 and 6 MHz the use of $e^2qQ/h \sim 2.6\text{--}2.8$ MHz gives acceptable ESEEM simulations. The adjustment of the asymmetry parameter η is more uncertain because it had only second-order effects on the spectral features; thus we have assumed the value $\eta = 0.2$ from the NQR data. A more detailed consideration would require to include a distribution of the spin-Hamiltonian parameters. Such a distribution is most likely present in the random network of the B_2O_3 structure. NMR (Ref. 4) data are consistent with the existence of small distribution of the nuclear quadrupole coupling values and a broader distribution of the η values. According to the theoretical analysis, for the cases under study the value of η has only minor influence on the ESEEM spectra. In addition, a

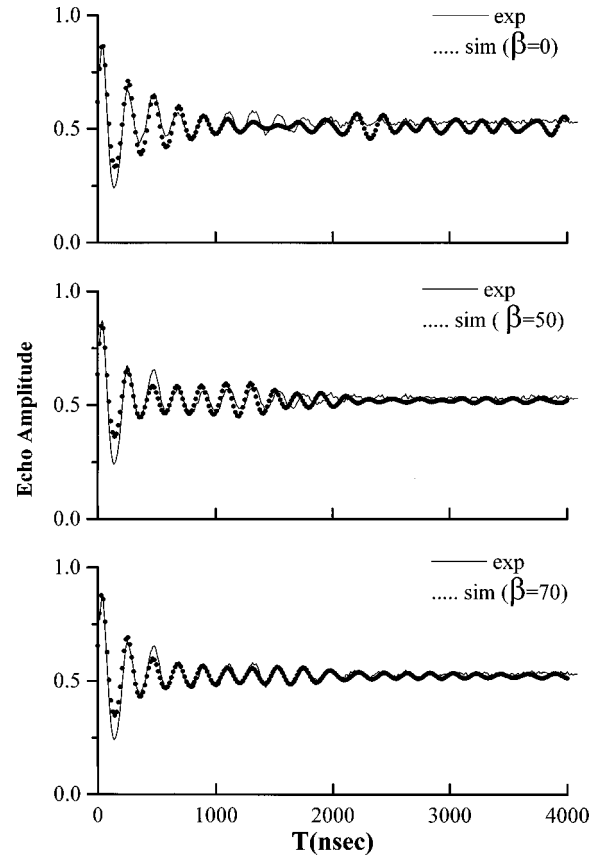


FIG. 14. Comparison between experimental ESEEM pattern (solid line) of B_2O_3 glass [taken from Fig. 10(A) for $\tau = 120$ ns] and calculated modulation patterns (filled circles) by using the spherical model for $N = 21$ ^{11}B nuclei and β values of 0° (top), 50° (middle), and 70° (bottom). The other calculation parameters are $\tau = 120$ ns, $\nu_I = 4.78$ MHz, $A_{\text{iso}} = 0$, $T = 0.35$ MHz, $e^2qQ/h = 2.6$ MHz, $\eta = 0.2$.

putative effect of a distribution of the η values is masked by the effect of other factors which might cause spectral broadening, like hyperfine anisotropy and instrumental dead time. In this context, the values for e^2qQ/h and η that we report here for the ^{11}B nuclei with A_{iso} of 2 and 6 MHz reflect only average values.

On proceeding to the simulations we see that by using the theoretical hyperfine couplings for the units A and C, Fig. 12, we get roughly similar ESEEM spectra with features at 1–2 and 7–8 MHz, Fig. 13. The theoretical hyperfine couplings for the structure B give a spectrum with a multitude of features between 4 and 6 MHz, Fig. 13.

The contribution of the weakly coupled ^{11}B nuclei is the dominant feature in the experimental spectrum. In the frequency domain, they give rise to the main feature at 4.7 MHz. The time-domain signal is more sensitive to the various coupling parameters for these weakly coupled nuclei. We find that coupling parameters resulting in viable simulations of the time-domain spectrum at $\tau = 120$ ns are restricted to cases with $A_{\text{iso}} \cong 0$ MHz. Nonzero values of the A_{iso} in the range < 0.5 MHz are readily discarded since they fail to reproduce even the gross features of the matrix ^{11}B modulation. The trade-off between the values of e^2qQ/h the anisotropic hyperfine coupling T and the number on the coupled

TABLE VI. ¹¹B nuclear coupling parameters [in MHz; T is $g_e g_n \beta_e \beta_n / (\hbar r_{\text{eff}}^3)$] used for the calculation of ESEEM spectra (the calculated spectra are displayed in Fig. 13).

Unit (A)	Unit (B)	Unit (C)	Matrix ¹¹ B nuclei
(A_{iso}, T)	(A_{iso}, T)	(A_{iso}, T)	$A_{\text{iso}} = 0$ MHz
(5.93, 0.42)	(-1.91, 0.8)	(6.57, 0.4)	$e^2 q Q / h = 2.8$ MHz
(6.22, 0.38)	(-1.90, 0.8)	(0.02, 0.20)	$T = 0.35$ MHz
(0.32, 0.10)	(-0.11, 0.18)	(0.16, 0.17)	$\nu_1 = 4.72$ MHz
(0.16, 0.12)	(-0.00, 0.18)		$\eta = 0.2$
	(-0.00, 0.2)		$N = 21$
	(-0.11, 0.2)		$\beta = 70^\circ$

¹¹B nuclei, N , restricts the range of their possible acceptable values. The effects of these parameters on the modulation have been separately analyzed in detail in the theoretical analysis of the ESEEM spectra, earlier in this paper. The best fit matching the modulation depth and the line shape of the experimental time-domain spectrum at $\tau = 120$ ns is shown in Fig. 14 (bottom trace, full circles). For comparison the experimental spectrum is displayed also. The simulated spectrum is calculated by using $N = 21$ ¹¹B nuclei with $T = 0.35$ MHz which in the point dipole approximation corresponds to an effective electron-nuclear distance $r_{\text{eff}} = 4.3$ Å. Trace M in Fig. 13 is the corresponding frequency domain spectrum. The full set of the simulation parameters is listed in Table VI.

The weak bump at 9.6 MHz in Fig. 13 (trace M) is a ‘‘combination line’’ due to the multiple nuclear coupling. The number of ¹¹B nuclei has a profound impact on the modulation depth which can vary up to 20% for T values between 0.35 and 0.38 MHz. In structural terms these results show that each paramagnetic oxygen is surrounded by $N = 21 \pm 4$ borons located at effective distances of 4.3 Å.

The value of the Euler angle β , i.e., the relative orientation between the z quadrupole and hyperfine axes, has a decisive impact on the modulation pattern. As it is shown in Fig. 14 by using the coupling parameters listed in Table VI, the best fit is achieved for $\beta = 70^\circ$ while other values like 0° or 50° lead to a mismatch of the late phases and/or the modulation depth. In nonirradiated B₂O₃ glass, experimental² and theoretical^{45,46} calculations show that the z principal axis of the ¹¹B quadrupole tensor must be perpendicular to the BO₃ triangle. Assuming a similar orientation for the matrix borons in the irradiated B₂O₃ glass, the ESEEM data show that for these matrix borons the z axis of the hyperfine coupling tensor lies close to the BO₃ plane.

In summary, this analysis shows that the matrix ¹¹B-nuclear couplings account for the main part of the experimentally observed modulation. The small differences observed between the experimental and the calculated spectrum in Fig. 14 are due to the fact that the experimental spectrum in addition to the matrix ¹¹B modulations contains two more contributions: one comes from the ¹⁰B ($I = 3$) nuclei and the second is due to the ¹¹B nuclei with A_{iso} 's of 2 and 6 MHz.

Their contribution can be better viewed in the frequency-domain spectra which are displayed in Fig. 13, where the various contributions in the total simulated spectrum are displayed together with the experimental spectrum (dashed line). The structural units A and C contribute mainly to the broad feature at 7–8 MHz, while unit B contributes at the central part of the spectrum. The detailed examination on the relative intensities of the spectral features in the composite simulated spectrum allows an attempt of a more quantitative analysis. For example, at close inspection, we see that the relatively sharp feature at 7.7 MHz in the spectrum of unit A cannot be resolved in the experimental spectrum. In this context we have scrutinized the possible quantitative combinations of the various subspectra, i.e., from units A , B , C , and the matrix borons, that simulate satisfactorily the experimental trace. The best fit is the spectrum displayed in Fig. 13 (solid line on the top) where the spectrum from the matrix borons has been combined with the subspectra from units I, II, III multiplied by 0.9, 0, 0.2 respectively. Strictly speaking, at the quantitative level the exact ratios of these factors have to be treated with caution; partial excitation, imperfection of the microwave pulses, and dead time are potential factors which could distort the ESEEM intensities.¹⁸ Nevertheless the comparative analysis might indicate that in B₂O₃ glass the structural units A and B might exist to a much less extent than unit C .

CONCLUSION

By using 1D-ESEEM and 2D-HYSCORE spectroscopy, weak ¹¹B hyperfine interactions and quadrupole couplings have been resolved in B₂O₃ glass. A detailed analysis of the time and frequency domain for the ESEEM spectra of a $I = 3/2$ system is presented. Based on molecular-orbital calculations the observed coupling parameters are discussed in terms of possible structural units. According to this analysis the ¹¹B atoms next to the paramagnetic oxygen bear considerable negative spin density which is due to spin polarization. The sign of the spin density for other ¹¹B atoms located on the boroxol ring depend on the structural details of its microenvironment. The quadrupole coupling tensor of the matrix ¹¹B nuclei has its z axis at 70° with respect to the hyperfine tensor. The ESEEM data show that the B₂O₃ glass certain structural units are preferable. The present analysis shows that the distribution of the unpaired spin density is sensitive to the short-range structure around the paramagnetic site and thus the ESEEM spectroscopy provides a sensitive tool for the study of this short-range structure in B₂O₃ glass. We consider that analogous structural information can be extracted for other amorphous materials by the proper use of ESEEM and molecular-orbital calculations.

ACKNOWLEDGMENTS

We thank GSRT and EC for funding under EIIET II 296, STRIDE 130 and 115.

- ¹J. Krogh-Moe, *Phys. Chem. Glasses* **3**, 101 (1962).
- ²G. E. Gellison and P. J. Bray, *J. Non-Cryst. Solids* **29**, 187 (1978); P. J. Bray, J. F. Emerson, D. Lee, S. A. Feller, D. L. Bain, and D. A. Feil, *ibid.* **129**, 240 (1991); R. E. Youngman and J. W. Zwanzinger, *ibid.* **168**, 293 (1994).
- ³For a review, see, P. J. Bray and E. J. Holupka, *J. Non-Cryst. Solids* **71**, 411 (1985).
- ⁴G. E. Jelison, L. W. Panek, P. J. Bray, and G. B. Rouse, *J. Chem. Phys.* **66**, 602 (1977).
- ⁵A. C. Hanon, D. I. Grimley, R. A. Hulme, A. C. Wright, and R. N. Sinclair, *J. Non-Cryst. Solids* **177**, 299 (1994).
- ⁶M. Massot, S. Souto, and M. Balkanski, *J. Non-Cryst. Solids* **182**, 49 (1995).
- ⁷F. L. Galeener and M. F. Thorpe, *Phys. Rev. B* **28**, 5802 (1983).
- ⁸F. L. Galeener, R. A. Barrio, E. Martinez, and R. J. Elliot, *Phys. Rev. Lett.* **53**, 2429 (1984).
- ⁹E. I. Kamitsos and M. A. Karakassides, *Phys. Chem. Glasses* **30**, 19 (1989).
- ¹⁰D. Kline, P. J. Bray, and H. M. Kritz, *J. Chem. Phys.* **48**, 5277 (1968); P. J. Bray, J. O. Edwards, J. G. O'Keefe, V. F. Ross, and I. Tatsusaki, *ibid.* **35**, 435 (1961).
- ¹¹G. E. Gurr, P. W. Modgometry, C. D. Knudson, and B. T. Gorres, *Acta Crystallogr., Sect. B: Struct. Crystallogr. Cryst. Chem.* **26**, 906 (1970).
- ¹²For a review, see D. L. Griscom, *J. Non-Cryst. Solids* **13**, 251 (1973).
- ¹³D. L. Griscom, P. C. Taylor, D. A. Ware, and P. J. Bray, *J. Chem. Phys.* **48**, 5158 (1968).
- ¹⁴M. C. R. Symons, *J. Chem. Phys.* **53**, 468 (1970).
- ¹⁵D. L. Griscom, P. C. Taylor, and P. J. Bray, *J. Chem. Phys.* **53**, 469 (1970).
- ¹⁶L. G. Rowan, E. L. Hahn, and W. B. Mims, *Phys. Rev. A* **138**, 4 (1965).
- ¹⁷S. A. Dikanov and Y. D. Tsvetkov, *ESEEM Spectroscopy* (CRC Press, Boca Raton, 1992).
- ¹⁸L. Kevan, in *Time Domain Electron Spin Resonance*, edited by L. Kevan and R. N. Schwartz (Wiley, New York, 1979), p. 279.
- ¹⁹P. Höfer, A. Grupp, H. Nedenführ, and M. Mehring, *Chem. Phys. Lett.* **132**, 279 (1986); P. Höfer, *J. Magn. Reson., Ser. A* **111**, 77 (1994).
- ²⁰J. J. Shane, P. Höfer, E. J. Reijerse, and E. J. De Boer, *J. Magn. Reson.* **99**, 596 (1992).
- ²¹S. A. Dikanov, R. I. Samoilova, J. A. Smieja, and M. K. Bowman, *J. Am. Chem. Soc.* **117**, 10 579 (1995).
- ²²V. Kofman, J. J. Shane, S. A. Dikanov, M. K. Bowman, J. Libman, A. Shanzer, and D. Goldfarb, *J. Am. Chem. Soc.* **117**, 12 771 (1995).
- ²³Y. Deligiannakis and A. W. Rutherford, *J. Am. Chem. Soc.* **119**, 4471 (1997).
- ²⁴E. J. Reijerse and C. P. Keijzers, *J. Magn. Reson.* **71**, 83 (1987).
- ²⁵J. Isoya, M. K. Bowman, J. R. Norris, and J. A. Weil, *J. Chem. Phys.* **78**, 1735 (1983); M. Narayana, L. Kevan, and S. Schlick, *ibid.* **86**, 196 (1982).
- ²⁶S.-H. Jang, H.-I. Lee, J. McCracken, and J. E. Jackson, *J. Am. Chem. Soc.* **115**, 1263 (1993).
- ²⁷R. Krimse, K. Kohler, U. Abram, R. Bottcher, L. Golic, and E. de Boer, *Chem. Phys.* **143**, 75 (1990).
- ²⁸G. Kordas, *Phys. Chem. Glasses* **38**, 21 (1997).
- ²⁹R. Kumaresean and D. W. Tufts, *IEEE Trans. Acoust., Speech, Signal Process.* **ASSP-30**, 833 (1982).
- ³⁰V. V. Kurshev, H. A. Buskmaster, and L. Tykarski, *J. Chem. Phys.* **101**, 10 338 (1994).
- ³¹K. Arai, S. Yamasaki, J. Isoya, and H. Namikawa, *J. Non-Cryst. Solids* **196**, 216 (1996).
- ³²M. J. S. Dewar and W. Thiel, *J. Am. Chem. Soc.* **99**, 4899 (1977); **99**, 5321 (1977).
- ³³GAUSSIAN 94, Revision D. 2, M. J. Frisch, G. W. Trucks, H. B. Schlegel, P. M. W. Gill, B. G. Johnson, M. A. Robb, J. R. Cheeseman, T. Keith, G. A. Peterson, J. A. Montgomery, K. Raghavachari, M. A. Al-Laham, V. G. Zakrewski, J. V. Ortiz, J. B. Foresman, J. Cioslowski, B. B. Stefanov, A. Nanayakkara, M. Challacombe, C. Y. Peng, P. Y. Ayala, W. Chen, M. W. Wong, J. L. Andres, E. S. Replogle, R. Gomperts, R. L. Martin, D. J. Fox, J. S. Binkley, D. J. Defrees, J. Baker, J. P. Stewart, M. Head-Gordon, C. Gonzalez, and J. A. Pople, Gaussian, Inc. Pittsburgh PA, 1995.
- ³⁴J. M. Fauth, A. Schweiger, L. Braunschweiler, J. Forrer, and R. Ernst, *J. Magn. Reson.* **66**, 64 (1986).
- ³⁵G. Gemperle, G. Aebli, A. Schweiger, and R. R. Ernst, *J. Magn. Reson.* **88**, 241 (1990).
- ³⁶The Euler angles relating the principal axes systems of the quadrupole and hyperfine coupling tensors are defined according to the convention of H. Margenau and G. M. Murphy, *The Mathematics of Physics and Chemistry*, 2nd ed. (Van Nostrand, New York, 1956).
- ³⁷W. B. Mims, *Phys. Rev. B* **5**, 2409 (1972); **6**, 3543 (1972).
- ³⁸T. Ichicawa, *J. Chem. Phys.* **83**, 3790 (1985).
- ³⁹D. Goldfarb and L. Kevan, *J. Chem. Phys.* **87**, 6323 (1987); K. Matar and D. Goldfarb, *ibid.* **96**, 6484 (1992).
- ⁴⁰K. Matar and D. Goldfarb, *J. Chem. Phys.* **96**, 6465 (1992).
- ⁴¹M. Heming, M. Narayana, and L. Kevan, *J. Chem. Phys.* **83**, 1478 (1985).
- ⁴²T. P. Das and E. L. Hahn, *Solid State Physics: Advances in Research and Applications* (Academic, New York, 1958).
- ⁴³J. A. Tossel, *J. Non-Cryst. Solids* **183**, 307 (1995).
- ⁴⁴M. Romanelli, M. Narayana, and L. Kevan, *J. Chem. Phys.* **80**, 4044 (1984); **83**, 4395 (1985).
- ⁴⁵A. A. Shubin and S. A. Dikanov, *J. Magn. Reson.* **52**, 1 (1983); **64**, 185 (1985).
- ⁴⁶C. Snyder, G. E. Peterson, and C. R. Kurkijian, *J. Chem. Phys.* **64**, 1569 (1976), and references therein.